In Situ Diagnostics and Role of Light-Induced Forces in Metal Laser Nanoprinting

Liang Yang, Aso Rahimzadegan, Vincent Hahn, Eva Blasco, Carsten Rockstuhl, and Martin Wegener*

Compared to 3D laser nanoprinting of polymers, the mechanisms in laser nanoprinting of metals are rather poorly understood. For the example of platinum investigated here, the printing process starts with the formation of metal nanoparticles by photo-reduction of metal salts in aqueous solution in a diffraction-limited laser focus. To investigate the printing process in situ, a weak continuous-wave probe laser is co-focused in addition to the focused femtosecond printing laser. The light of the probe laser is backscattered off the emerging metal structures, and recorded with a temporal resolution of 1 μs. It is found that the formed metal nanoparticles are quickly ejected from the focus on a timescale of some 10 μs. Once a nanoparticle randomly adheres to the substrate surface, it serves as a seed from which structures can be built-up. The following nanoparticles are sintered onto that seed to form a metallic voxel on a timescale of some 10 ms. By polarization-dependent experiments and full-wave optical simulations, it is shown that light-induced forces onto the nanoparticles play a significant role. The improved understanding of the microscopic processes in metal nanoprinting is a prerequisite for further process optimizations and applications, for example in terms of printed optoelectronics.

1. Introduction

Multi-photon 3D laser micro- and nanoprinting of polymers[1,2] has become a commercially available and routine research tool in optics,[3–5] mechanics,[6–8] biology,[9,10] and micro-robotics,[11–15]

and is starting to enter the industrial market. Even multi-material multi-photon 3D printing is emerging.[16–18] However, it is fair to say that multi-photon 2D or 3D printing of metals, which has many potential applications in electronics and optoelectronics, falls behind in terms of structure quality and printing speed.[19,20] Previous experiments include the noble metals gold,[21–27] silver,[28–39] platinum,[40,41] and palladium.[40,42,43] For platinum, especially high-quality planar sub-micrometer structures have been realized,[40] exhibiting electrical conductivities close to the bulk value.

While one might suspect that the mechanisms at work in the printing of polymers and metals share similarities, it has become increasingly evident that the mechanisms are indeed different.[44–48] Previously, optical in situ diagnostics of the polymerization process in 3D multi-photon printing of polymers has significantly helped to understand the underlying microscopic processes and timescales.[49,50] However, such experiments are yet missing for the multi-photon laser nanoprinting of metals.

Earlier work has discussed the dynamics of the reduction of gold nanoparticles in solution based on a transient grating approach,[51] and the formation of millimeter-sized objects

L. Yang, V. Hahn, E. Blasco, C. Rockstuhl, M. Wegener
Institute of Nanotechnology
Karlsruhe Institute of Technology (KIT)
76128 Karlsruhe, Germany
E-mail: martin.wegener@kit.edu

L. Yang, V. Hahn, M. Wegener
Institute of Applied Physics
Karlsruhe Institute of Technology (KIT)
76128 Karlsruhe, Germany

A. Rahimzadegan, C. Rockstuhl
Institute of Theoretical Solid State Physics
Karlsruhe Institute of Technology (KIT)
76131 Karlsruhe, Germany

E. Blasco
Institut für Organische Chemie
Ruprecht-Karls-Universität Heidelberg
Im Neuenheimer Feld 270, 69120 Heidelberg, Germany

E. Blasco
Centre for Advanced Materials (CAM)
Ruprecht-Karls-Universität Heidelberg
Im Neuenheimer Feld 225 and 270, 69120 Heidelberg, Germany

from silver nanoparticles based on X-ray probing,[52] both for single-photon absorption in vast volume. Here, we present time-resolved in situ diagnostics experiments for multi-photon laser printing of platinum. These experiments are based on the time-resolved backscattered light of a weak continuous-wave probe laser that is co-focused with the femtosecond writing laser. The temporal resolution for measuring the backscattered light is chosen below the critical one to track the dynamics of the metal nanoparticle formation. In addition, we find that the printed structures show a remarkable dependence on the polarization of the writing laser. This dependence indicates the importance of optical forces in the assembly process of the nanoparticles. Therefore, we perform supporting full-wave optical simulations to quantify these forces for individual platinum nanoparticles and pairs of nearby platinum nanoparticles under the conditions of our experiments. The dynamics triggered by these forces provides further understanding of the writing process.
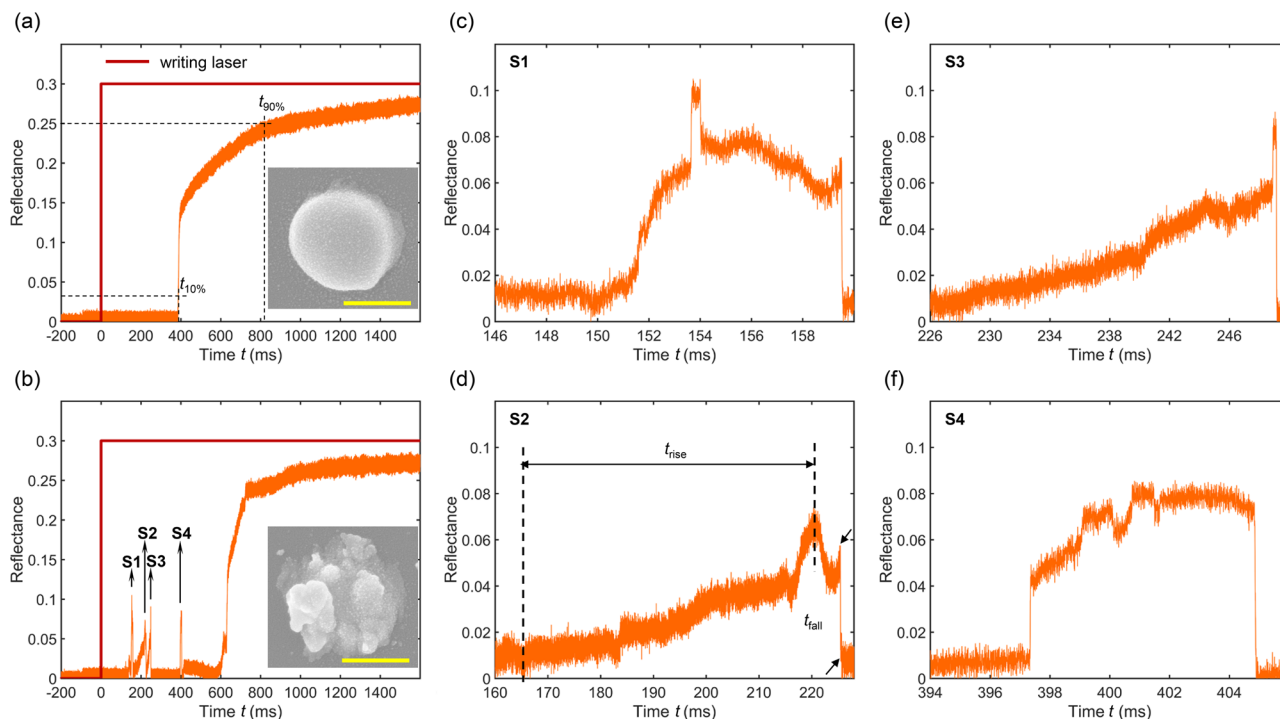
2. Experimental Results

To detect the metal reduction process in small volumes and on the timescale of microseconds or less, a separate continuous-wave (cw) probe laser at 675 nm wavelength is introduced into a multi-photon metal reduction printing system. This printing system builds on a mode-locked femtosecond (fs) laser oscillator (Chameleon, Coherent) emitting at a center wavelength of 780 nm (**Figure 1**a). The fs laser and the probe laser are combined by a dichroic mirror and focused onto the interface between a silanized glass substrate and the ink (see methods and materials section). A photodiode with a bandwidth of 5.5 MHz detects the backscattered probe light. A small contribution to this signal stems from the light reflected by the refractive index difference between the glass substrate and the ink. It is visible in all the data that we present here. A more interesting contribution stems from platinum nanoparticles or printed platinum dots or lines. The backscattered signal is normalized to the reflection signal that we obtain by moving a large-footprint gold film with a thickness of 120 nm into the focus (see inset in Figure 1a). Taken the refractive index of cover glass and gold as 1.517 and $0.108 + 4.05i$,[53] we calculate the reflectance from the glass–gold interface to be 96.54%. Via this normalization, we obtain a dimensionless and physically meaningful reflectance signal. By definition, this signal lies in the interval [0%, 100%]. This gold coating is only used in the reference experiment, and it is not used in the in situ experiments during laser printing. We record in parallel the trigger signal going to the writing laser. An oscilloscope records both signals. The sampling time is set to one microsecond, which is sufficiently fast to resolve all transients reported below. The rising edge of the writing laser envelope serves as the trigger signal for the oscilloscope recording. To eliminate possible crosstalk from the writing laser to the photodiode for the probe laser signal, a 675 nm band-pass filter (Chroma Technology) is placed immediately in front of the photodiode. To probe the region of the writing laser focus with the probe laser, the two foci are carefully co-aligned to the same position in the three-dimensional space (Figure 1b). In these measurements, we scan a 150 nm diameter platinum bead through the focus and record the backscattered light. We determine a full width at half maximum (FWHM) focus diameter of
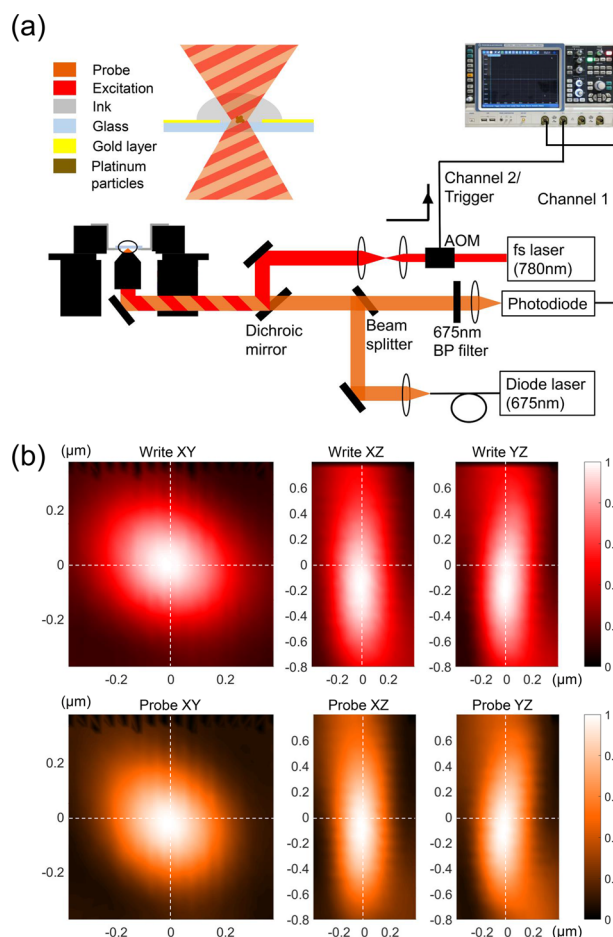
Figure 1. Experimental method and measured writing and probe laser foci. a) A mode-locked femtosecond laser oscillator emitting at a center wavelength of 780 nm is used as the writing laser. A separate continuous-wave laser at 675 nm wavelength is introduced as a probe laser. Writing laser and probe laser are combined by a dichroic mirror and focused onto the interface of a silanized glass substrate and the ink. A photodiode is used to detect the backscattered probe light. The excitation signal sent to the writing laser and the detected signal are collected with an oscilloscope. A band-pass filter around 675 nm wavelength is placed in front of the photodiode to eliminate possible crosstalk from the fs laser. Inset: the glass substrate is partially coated with a 120 nm gold layer (not to scale, the gold layer is actually far away from the laser focus). The reflectance from the glass–gold interface is measured experimentally and calculated to be 96.54%. All the backscattered signals in laser writing experiments are normalized based on the results from the glass–gold interface. b) Measured foci of the writing and the probe laser, respectively. Cuts are shown for the xy-, the xz-, and the yz-plane. The data for the two foci are shown in the same coordinate system. This allows to assess how well the two laser foci are aligned with respect to each other. In the xy-plane, we determine a FWHM of 400 and 350 nm for the writing laser and the probe laser focus from these data, respectively.

400 and 350 nm for the writing laser and the probe laser, respectively.

To explore the metal reduction process, we start with point-exposure experiments. The sample is static, and the focus of the writing laser as well as of the probe laser are fixed to the glass-ink interface. The sampling of the photodiode signal starts at time −200 ms and lasts until time 1600 ms, which is the upper bound

**ADVANCED
SCIENCE NEWS**

www.advancedsciencenews.com

LASER
& PHOTONICS
REVIEWS

www.lpr-journal.org

Figure 2. Monitored curves and spikes. a) shows an example of a regular trace of the detected signal. After hundreds of milliseconds incubation period, the reflectance signal steeply rises and then increases further over a longer time span until eventually a plateau is reached. $t_{10\%}$ and $t_{90\%}$ correspond to the time that the signal reaches 10% and 90% of its maximum. b) shows an example of an irregular trace of the detected signal, in which a set of sharp temporal spikes is observed before the rise leading to the plateau. The insets of (a,b) are scanning electron micrographs of written platinum particles corresponding to the same events. The scale bars are 500 nm. b–d) are the resolved patterns of spikes S1, S2, S3, and S4, respectively after zoom-in. In (d), the rise time, t_{rise}, and the fall time, t_{fall}, are defined. For these experiments, the laser power has been 40% P_0.

up to which we trace the dynamics of the processes. As pointed out above, the oscilloscope sampling rate is 1 µs^{-1}. It implies that 1.8 million data points are sampled in each point-exposure experiment. Typical measured curves are shown in **Figure 2**a,b. From −200 to −100 ms, both the writing laser and the probe laser are off. At −100 ms, the probe laser is switched on with a power of 12 µW, and a small probe signal is indeed visible in the data. As pointed out above, this signal stems from the reflection of the probe laser off the glass-ink interface. At time 0 ms, the writing laser is switched on, and the laser-induced reduction can start in the writing laser focus. After a certain "incubation period", the detected signal rapidly increases, followed by a plateau, which can reach reflectance values as large as 28%. We will later assign these signals to backscattering from platinum nanoparticles and printed platinum structures, respectively.

Several control experiments are performed to rule out other sources of the increased signal measured from the photodiode. First, to rule out the effect of laser reduction by the probe laser itself, the probe laser is switched on for 900 s (15 min) while the writing laser is completely switched off. No increase of the detected signal is observed (Figure S1, Supporting Information). This observation is expected because the power of the probe laser is two orders of magnitude lower than that of the writing laser. Second, experiments with the writing laser switched on and the probe laser completely switched off are additionally performed. Again, no detectable signal is found. The latter control experiment rules out that the photodiode signal is, e.g., due to thermal

(Planck) radiation generated by the writing laser heating the focal region, e.g., by absorption of light from the writing laser (Figure S2, Supporting Information). To avoid misunderstandings, we emphasize that we do not claim that heating plays no role. We only state that thermal radiation from the focal region does not contribute to the discussed probe signal.

Two examples of measured traces are shown in Figure 2a,b. Panel a shows a regular behavior whereas that in panel b is somewhat irregular. Both have in common that the reflectance signal rises only hundreds of milliseconds after the writing laser has been switched on. We refer to this time delay as the incubation period. In Figure 2a, the reflectance signal steeply rises at around 400 ms and then increases further over a longer period until eventually a plateau is reached. The behavior in Figure 2b is different. Here, we observe a set of sharp temporal spikes before the rise leading to the plateau. These spikes appear at random moments in time and exhibit differently curved shapes. To further investigate these spikes, we zoom into these regions in Figure 2c–f. Typically, the spikes have a rise time on the orders of some ten milliseconds. Beyond that, it is difficult to unambiguously define time constants or time scales for such irregular behaviors. In an attempt to further quantify the behavior, we define the rise time, t_{rise}, as illustrated in Figure 2d. Here, the rise is relatively well behaved, which cannot be said about the much more irregular behaviors found in Figure 2c,e,f. All of these traces have in common that the reflectance signal, after some complex rise, exhibits a sharp drop toward small reflectance values. We emphasize that

none of these signatures is due to measurement noise. Remarkably, the sharp drop occurs on a much shorter timescale than the rise. We define the fall time t_{fall} as illustrated in Figure 2d. The fall times are in the range of tens of microseconds, nearly three orders of magnitude shorter than the rise times. After a spike has passed, the signal reaches a low steady level. After that, a further peak may occur or we observe the aforementioned continuous increase toward a plateau (Figure 2a,b). We will come back to the interpretation of these findings in the discussion section. However, it is already fairly evident from the raw data that something sudden must happen to the platinum nanoparticles at the points of rapid reflectance signal drop.

Figure 2a,b has already shown a rather different behavior—although both have been taken under nominally identical conditions. To further illustrate the spread in the observable temporal dynamics, we summarize the signals from 200 point-exposure experiments with the same experimental parameters in Figure 2 as in Video S1 in the Supporting Information. From these raw data it is obvious that the start of the platinum laser printing has a pronounced random component.

It is interesting to correlate the discussed in situ reflectance signal data with the images of the corresponding printed platinum objects. We emphasize that these electron micrographs, shown as insets in Figure 2, correspond to the same events. For example, Figure 2a exhibits a platinum particle with spherical geometry and with a smooth surface. The corresponding reflectance signal versus time is smooth and does not exhibit any of the aforementioned sharp spikes. In contrast, whenever spikes are observed in the reflectance signal versus time, such as, for example, in Figure 2b, the corresponding resulting platinum particles are very rough and show irregular protrusions on top of the primary particles.

Apart from the irregular spikes in the in situ reflectance signal, the main observations so far are the finite incubation time and the finite rise time. These observations correlate positively with observations that we and others have made previously in the writing of platinum structures without in situ diagnostics.[40,54] When, e.g., writing a line, we always had to wait at the starting point for a while to obtain a line that starts at the starting point. This waiting time depends on the laser power. Moreover, when writing lines, the scan speed could not exceed a particular value. Otherwise, the lines showed interruptions. It is suggestive to connect this speed limitation with the finite rise time discussed above. If the time between two successive point exposures in a line is comparable to or even shorter than the rise time, the two points are no longer connected. This interpretation is confirmed by experiments in which we print metal lines at different focus velocities (see Figure S3, Supporting Information).

Therefore, it is interesting to further investigate the incubation time and the rise time by analyzing the data statistically. For that purpose, we repeat experiments like the ones shown in Figure 2 for 100 times and analyze the incubation time $t_{10\%}$ and the characteristic rise time $t_{90\%} - t_{10\%}$. As these times are also expected to depend on the laser power, we systematically vary the laser power. We define $P_0 = 3.5$ mW as the reference power and relate all other powers to this value. Corresponding results are summarized in **Figure 3**a,b. For each power, we have analyzed at least 100 raw data sets.

In Figure 3a, when increasing the laser power from 30% to 70% of the reference power, the mean incubation times decrease from around 390 to 200 ms. This decrease is expected as larger laser powers correspond to larger rates and larger yield of photoreduction, leading to a more rapid generation of platinum nanoparticles. In addition, for low powers approaching 30% relative power, the relative widths of the distributions are larger than for large powers. This behavior is also expected because 30% is close to the minimum threshold, below which no platinum particles are generated at all.

The mean rise times, $t_{90\%} - t_{10\%}$, analyzed in Figure 3b show little if any dependence on the laser power. The mean rise times are roughly constant at around 600 ms. Only the widths of the rise-time distributions increase with laser power increasing from relative 30% to 70%. This finding indicates some increased level of randomness at larger powers. We will come back to the interpretation of these findings in the discussion part.

Above, we have already pointed to the connection of these rise times and the maximum possible focus scanning speed. The latter can be crudely estimated by taking the typical focus diameter and dividing it by the rise time. We obtain values on the order of 1 µm s^{-1}. Clearly, taking only a fraction of the rise time leads to somewhat larger estimated maximum focus speeds approaching 10 µm s^{-1}. Such values in the range 1–10 µm s^{-1} are consistent with the maximum focus scanning speeds reported in a large number of publications by different groups.[21,24,26,28–30,36,40]

In Figure 3c,d, we statistically analyze the rise and fall times, t_{rise} and t_{fall}, associated with the sharp spikes discussed before (Figure 2b). The mean rise time is about 20 ms, whereas the mean fall time is around 40 µs. Notably, the mean fall time is nearly three orders of magnitude shorter than the mean rise time. The rise time in the spikes is more than one order of magnitude smaller than the $t_{90\%} - t_{10\%}$ times of around 600 ms discussed above. This suggests that different mechanisms underlying these different time constants are at work. Both, rise and fall times, show little if any significant dependence on the relative laser power.

So far, we have exclusively discussed experiments corresponding to point exposures. We now turn our attention to the laser writing of platinum lines and corners. Results are shown in **Figure 4**a,b, respectively. In all of these experiments, the laser focus stays still at the starting point for 560 ms (first vertical dashed lines in Figure 4a,b) and is then moved over a distance of 10 µm at a focus speed of 10 µm s^{-1}. The used laser power is 40%P_0. In the line scanning in Figure 4a, we again find small spikes before the rise of the reflectance signal at around 500 ms. During the writing of the line, the reflectance signal fluctuates. We emphasize once again that these fluctuations are not due to noise from the measurement but are rather fluctuations due to the printing process itself. For the corner writing in Figure 4b, the start is roughly similar, apart from the usual fluctuations. When turning to write along the orthogonal direction, which starts at the second vertical dashed line, the reflectance signal drops significantly. The reflectance signal stays at this low level. We emphasize that we actually scan the sample with respect to the fixed laser focus, such that the two laser foci, the writing laser and the probe laser, stay aligned to each other. We can therefore rule out that the signal drop at the corner is an experimental artifact.
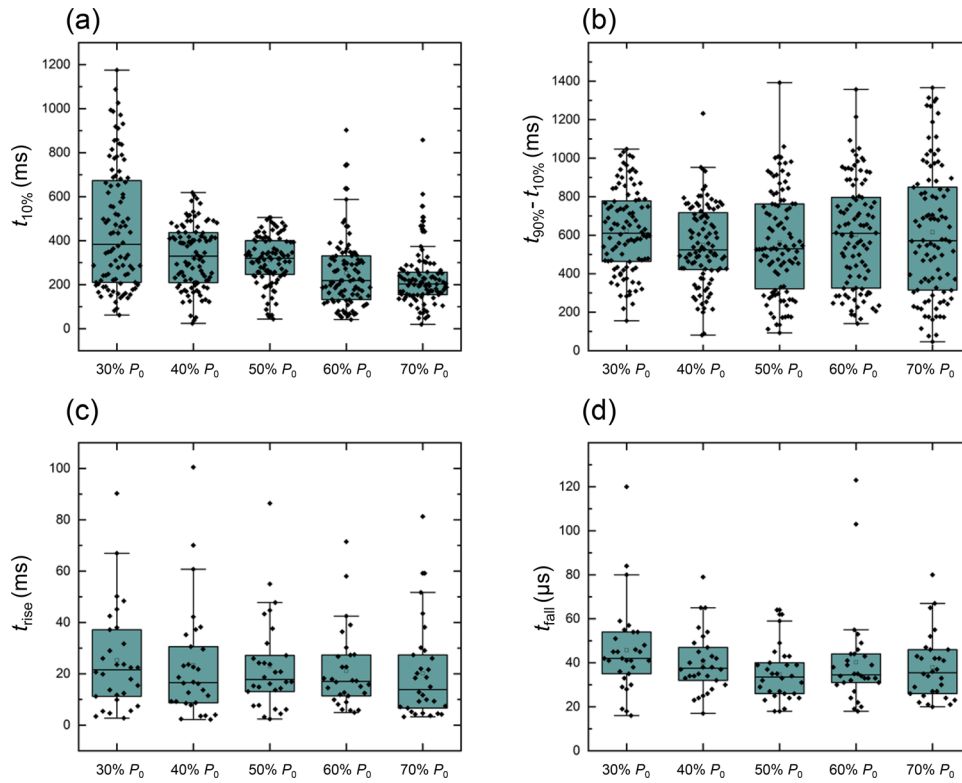
Figure 3. Statistical analysis of the measured in situ signals. a) Point-exposure experiments are conducted for different laser powers, ranging from 30% P_0 to 70% P_0. For each power, the incubation period is analyzed by $t_{10\%}$ from 100 raw data sets. b) The characteristic rise time $t_{90\%} - t_{10\%}$ is analyzed the same way as $t_{10\%}$. c) The rise time, t_{rise}, and d) the fall time, t_{fall}, of spikes are also statistically analyzed for each laser power.
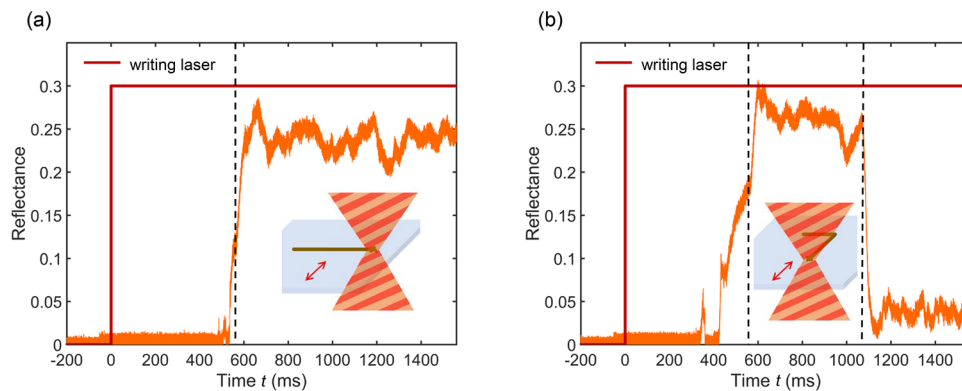
Figure 4. Monitoring the process of line writing and corner writing. a) The laser focus stays still at the starting point for 560 ms (first dash line). Thereafter, the laser focus scans for a distance of 10 µm with a speed of 10 µm s^{-1} and laser power of 40% P_0. The writing process lasts for 1 s. b) Different from line writing, in corner writing experiments, the writing direction turns to the orthogonal direction at a position of 5 µm (the second vertical dashed line). The reflectance signal drops significantly at the turning point and stays at a low level until the end of writing. The laser scanning directions are illustrated in the insets, and the laser polarization directions are marked by the red double-arrows.

At first sight, the signal drop seems to violate the symmetry of the problem as the x- and y-direction appear to be equivalent. However, they are not equivalent because the polarization of the writing laser breaks the symmetry. The double arrows indicate the writing laser polarization in Figure 4a,b. This difference in reflectance signal for the two orthogonal directions suggests that the morphology of the printed lines is different for lines parallel and perpendicular to the writing laser polarization, respectively.

To further investigate this unexpected finding, we have inspected lines for different laser polarizations by electron microscopy. Results are shown in **Figure 5**. In panels a–c, we find stripes on the platinum lines which correlate positively with the orientation of the linear laser polarization, which is schematically shown in the left column. To ensure that no other symmetry breaking mechanism is at work, we also laser write and inspect corners and lines that are written along the

2100411 (5 of 13)
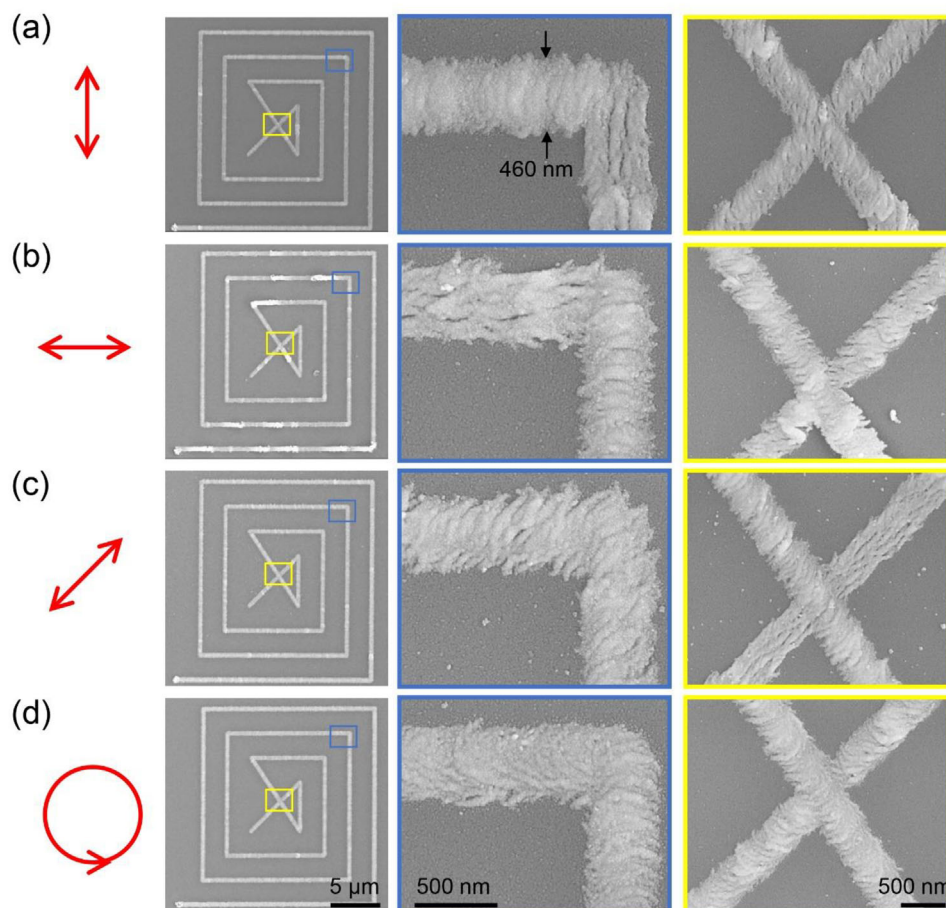
Figure 5. Scanning electron micrographs of platinum patterns written using a fs laser for different polarizations. a–c) are platinum patterns from horizontal, vertical, and 45° linear polarization (see red double-arrows on the left). To make sure that no other symmetry breaking mechanism is at work, corners (third column) and lines written along the diagonals (fourth column) are inspected. Stripes on the platinum lines correlate positively with the orientation of the linear laser polarization. d) is a platinum pattern written with circular polarization. Different from stripes for linear polarization, arc-like strokes are observed. For these experiments, the laser power has been 28% P_0 and the scan speed 1 µm s^{-1}.

diagonals. The correlation between the stripes and the laser polarization is evident from the data shown in Figure 5, especially from the magnified electron micrographs in the third and fourth columns. In Figure 5d, we aim at circular polarization of light by introducing a quarter-wave plate into our setup. Here, the surface morphology of the platinum lines is different from that for linear polarization. We instead find arc-like structures. However, it should be mentioned that the polarization in the focus is not perfectly circular due to the polarization dependence of elements behind the quarter-wave plate in the beam path. For all of the structures shown in Figure 5, we find that the lines are composed of densely packed platinum nanoparticles with a diameter below 20 nm (also see Figure S4, Supporting Information). It is suggestive to assume that these nanoparticles have been formed during the writing process and have aggregated together by some means. Whatever the precise mechanism, it is important to point out that it is evident from the experimental data alone that light-induced forces must play an appreciable role here. Otherwise, we see no other mechanism that would lead to structures aligned with the writing-laser polarization. This finding asks for full-wave optical simulations of the light forces at

work under the conditions of our printing experiments. We will present such calculations below. In the discussion section, we will interpret the experimental data together with the simulation data.

Before turning to the simulations, we note two aspects. First, related polarization-dependent effects have previously been observed in laser printing experiments on large-area silver structures under conditions of multi-photon reduction.[32] Second, our laser-printed platinum lines do not exhibit such pronounced stripes for all conditions. In Figure 5, we have shown data for laser powers close to the threshold and scanning at a speed of 1 µm s^{-1}. At higher laser powers, the resulting platinum lines reveal a much smoother surface (Figure S4, Supporting Information). However, the line morphology is still affected by the relative orientation of laser polarization and scanning direction (Figure S4, Supporting Information). For applications where smooth lines may be aimed-at, circular polarization of the writing laser and large scan speeds are favorable. We have emphasized low writing laser powers in Figure 5 because these data give the clearest hints toward the underlying mechanisms.
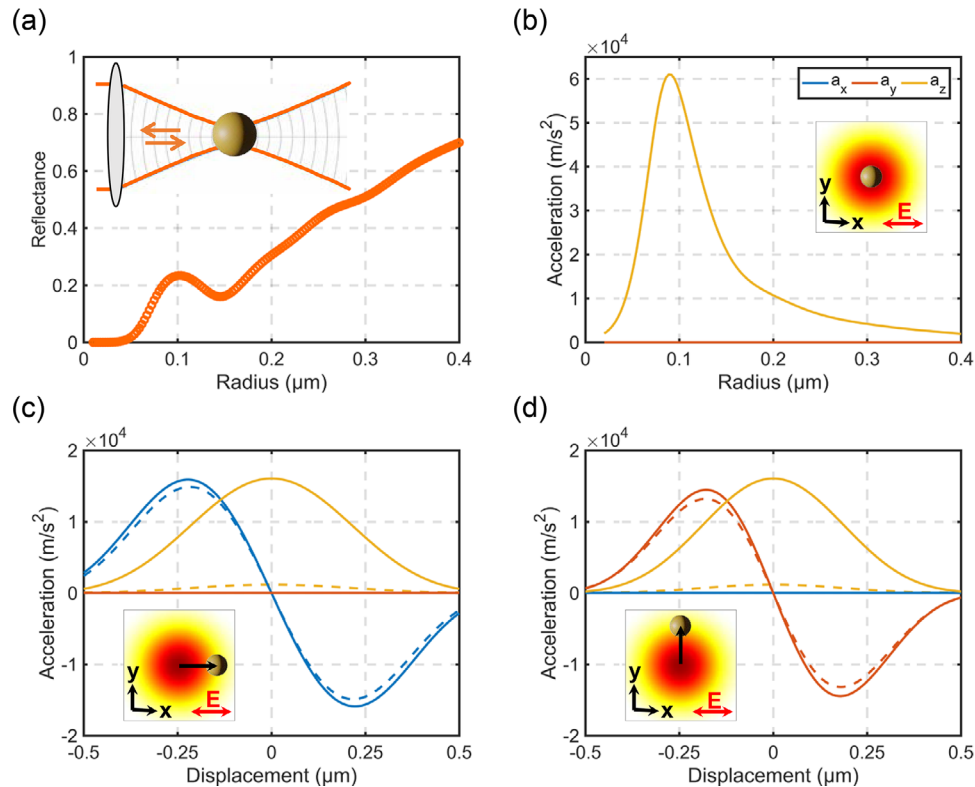
Figure 6. Reflectance from and exerted force on a single platinum nanosphere embedded in water. a) The reflectance from the nanoparticle in the focus of the fundamental transverse Gaussian beam as a function of the nanosphere radius for a beam waist of 300 nm at a wavelength of $\lambda = 675$ nm. The exerted acceleration on b) a single nanoparticle in the focus as a function of the nanoparticle radius and c,d) outside the focus as a function of the displacement from the center (radius of 10 nm) at a wavelength of $\lambda = 780$ nm. The insets illustrate the shown displacements. Nanospheres with a radius of 10 nm (dashed) and 50 nm (solid) are considered. The red double-arrows show the direction of the electric field polarization in the insets.

3. Calculated Optical Forces and Scattering

To aid the interpretation of the measured reflected probe signal ($\lambda = 675$ nm, beam waist = 340 nm) from the gradually growing platinum nanoparticles, we simulate the backward scattering of light off a platinum sphere depending on its radius by utilizing a multipolar method.[55–57] In the multipolar method, the incident and scattered fields are expanded into vector spherical harmonics (VSH) and, hence, are represented by their VSH coefficients. In this spherical basis, the optical response of a sphere can be calculated analytically (well known as the Mie coefficients[58,59]), and the scattered light coefficients can be derived from the incident field coefficients. For the simulations, we have assumed that light impinges onto the particle in the form of a fundamental transverse Gaussian beam (TEM$_{00}$). As the beam waist of the Gaussian beam is smaller than the wavelength, the paraxial approximation is not valid.[60] Therefore, we use a fifth-order corrected beam as originally proposed in References 61 and 62. A fifth-order correction for the beam at hand has an average relative error of around 1% and a maximum relative error of less than 20%.[61] For the entire analysis of this section, we consider a refractive index of $n = 1.33$ for the surrounding water. The refractive index of platinum at $\lambda = 675$ nm is $0.48 + 6.62i$.[63]

To derive the reflectance from a single particle using the multipolar analysis and the Mie theory, we have calculated the scattered field in a collection window that corresponds to the numerical aperture of the objective (i.e., NA = 1.25) at a distance of several wavelengths. The reflectance is then calculated as the ratio of the backward reflected power ($\theta = 180°$) to the incident power (i.e., $P_{in} = 2.5$ mW). The results are shown in **Figure 6**a. We have used a multipolar order of up to 10 to obtain numerically converged results for the multipolar analysis.

In the next step, we calculate the optical acceleration (force/mass F/m) exerted on a single platinum nanoparticle for a Gaussian beam of wavelength $\lambda = 780$ nm with a beam waist of 340 nm and a power of 2.5 mW, both in focus and out of focus. This step helps to understand the importance of gradient forces and the dynamics of the single spheres inside the surrounding water. For the optical-force calculations, we again use the multipolar analysis. The Maxwell stress tensor required for the force evaluation is calculated in the VSH basis in this approach. Then, the expression for the optical force contains the incident and scattered VSH coefficients,[55] and no surface integrals are required.[55,57,62] The mass density of the platinum, which is needed to compute the mass via the nanoparticle radius, is taken as 21.45 g cm^{-3}.[64] The simulated results are shown in Figure 6b–d. Figure 6b shows the optical acceleration exerted by the focused Gaussian beam along the x, y, and z-axes as a function of the platinum nanosphere radius. The peak at around a radius of 100 nm is especially important to notice. This peak is also seen in the reflectance data in Figure 6a. Note that the mass of the nanoparticle increases proportional to the cube of the nanoparticle radius.

Hence, the acceleration is generally decreasing after this peak. In Figure 6c,d, the optical acceleration in the focal plane ($z = 0$) but outside the focus ($x \neq 0$ and $y \neq 0$) is calculated for a single nanosphere of radius 10 and 50 nm, respectively. The polarization of the electric field is shown in the insets. The displacement along x and y are similar although slightly different in strength. This difference can be attributed to a slight asymmetry of the Gaussian excitation. An important finding of our calculations shown in Figure 6 is the dominance of the gradient forces outside the focus for smaller spheres compared to larger spheres. The exerted gradient accelerations are almost the same for both spheres. However, the acceleration along the wave propagation axis (z-direction) is much smaller for small spheres. This small pushing force for the small dipolar nanoparticle is linked to the small real part of the Mie coefficients compared to their imaginary parts, i.e., $\Re(a_1) < \Im(a_1)$, where a_1 is the electric-dipole Mie coefficient. The refractive index of platinum at $\lambda = 780$ nm is $0.56+7.84$i.[63]

In the next step, the interaction and the dynamics of a pair of platinum nanospheres are investigated. These calculations relate to the experimental data shown in Figure 5, where we have found a polarization dependence of the printed lines. Due to symmetry of the nanosphere and the isotropic surrounding, the response of a single particle to the Gaussian excitation does not show a noticeable polarization dependence. Therefore, we consider pairs of nanospheres. For this purpose, we continue to solve the full-wave Maxwell equations as a multipole scattering problem among the two nanospheres.[56,65] Comparable to ordinary Mie theory,[58] we expand all involved fields in frequency space using VSH considering the center positions of the nanospheres, $\mathbf{R}_1$ and $\mathbf{R}_2$, as the center of the coordinate system describing the scattering problem as seen from each particle. We expand, in particular, the external illumination impinging on each nanosphere and their scattered fields in the local coordinate systems of the respective nanospheres. The VSH coefficients of either the incident or the scattered field are collected in the vector, $\mathbf{q}_{ext}^{1/2}$ and $\mathbf{b}^{1/2}$, respectively. The superscript labels the considered sphere. For an isolated sphere, the relation between the scattered and the incident field is given as

$$\mathbf{b} = \overline{\overline{\mathbf{T}}} = \mathbf{q} \tag{1}$$

with $\overline{\overline{\mathbf{T}}}$ being called the T or transition matrix.[66] For a sphere, for which the VSH do not couple thanks to the high symmetry of the object, the T matrix is diagonal. In essence, the diagonal contains the Mie coefficients. Regarding the two nanospheres, we consider the incident field on each nanosphere as a superposition of the external illumination and the scattered field from the other nanosphere as

$$\begin{bmatrix} \mathbf{q}^1 \\ \mathbf{q}^2 \end{bmatrix} = \begin{bmatrix} \mathbf{q}_{ext}^1 \\ \mathbf{q}_{ext}^2 \end{bmatrix} + \begin{bmatrix} 0 & C(-\mathbf{R}_2) \\ C(-\mathbf{R}_1) & 0 \end{bmatrix} \begin{bmatrix} \mathbf{b}^1 \\ \mathbf{b}^2 \end{bmatrix} \tag{2}$$

where $C(-\mathbf{R}_m)$ is the translation coefficient matrix, translating the scattered field from particle m in its coordinate system into an incident field in the coordinate system of particle n. Details of this matrix can be found in the literature.[56] Now plugging in that expression into the original expression for the scattered field

from each particle, we arrive at

$$\begin{bmatrix} \mathbf{b}^1 \\ \mathbf{b}^2 \end{bmatrix} = \begin{bmatrix} \overline{\overline{\mathbf{T}}}_1 & 0 \\ 0 & \overline{\overline{\mathbf{T}}}_2 \end{bmatrix} \times \left\{ \begin{bmatrix} \mathbf{q}_{ext}^1 \\ \mathbf{q}_{ext}^2 \end{bmatrix} + \begin{bmatrix} 0 & C(-\mathbf{R}_2) \\ C(-\mathbf{R}_1) & 0 \end{bmatrix} \begin{bmatrix} \mathbf{b}^1 \\ \mathbf{b}^2 \end{bmatrix} \right\} \tag{3}$$

This is a system of linear equations that can be recast into

$$\begin{bmatrix} \mathbf{b}^1 \\ \mathbf{b}^2 \end{bmatrix} = \left\{ \begin{bmatrix} \overline{\overline{\mathbf{I}}} & 0 \\ 0 & \overline{\overline{\mathbf{I}}} \end{bmatrix} - \begin{bmatrix} \overline{\overline{\mathbf{T}}}_1 & 0 \\ 0 & \overline{\overline{\mathbf{T}}}_2 \end{bmatrix} \begin{bmatrix} 0 & C(-\mathbf{R}_2) \\ C(-\mathbf{R}_1) & 0 \end{bmatrix} \right\}^{-1}$$
$$\begin{bmatrix} \overline{\overline{\mathbf{T}}}_1 & 0 \\ 0 & \overline{\overline{\mathbf{T}}}_2 \end{bmatrix} \begin{bmatrix} \mathbf{q}_{ext}^1 \\ \mathbf{q}_{ext}^2 \end{bmatrix} \tag{4}$$

and which can easily be solved by matrix multiplications. We stress that information concerning the particles is contained in the T matrix, information concerning their location is contained in the translation matrix, and information concerning the external illumination is contained in the dedicated vector. Once the coefficients expanding the scattered and incident fields are known, all the relevant quantities can be directly calculated.[59]
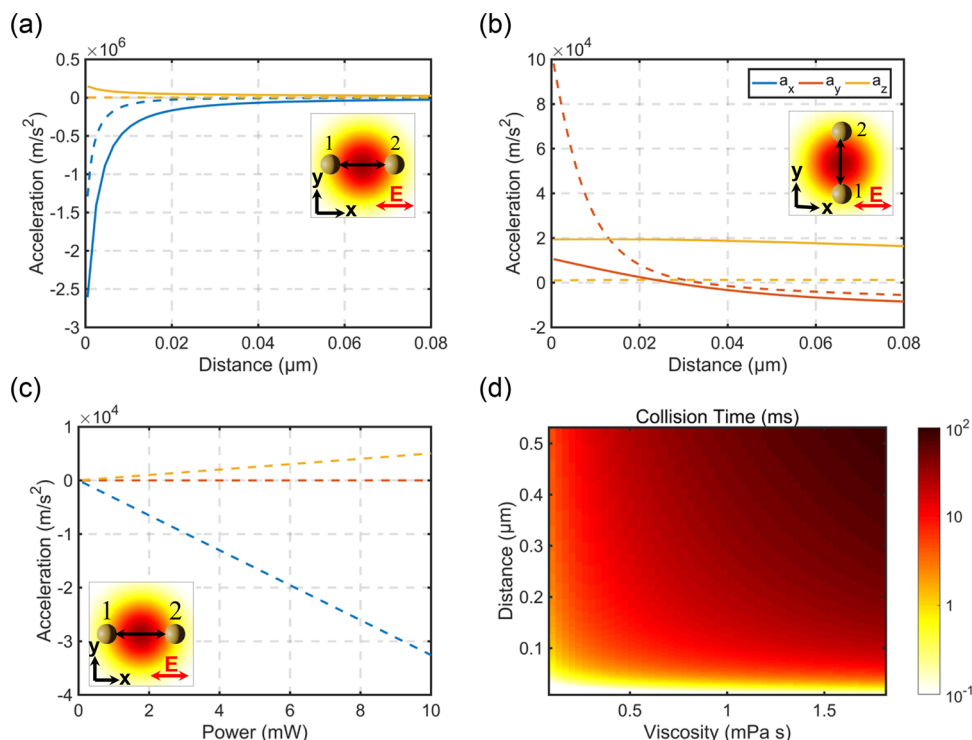
In the following, we assume that the pair of nanospheres is arranged symmetrically with respect to the central focus, as shown in the inset of **Figure 7**. Because of this symmetry, we only show the results for nanoparticle #2. In Figure 7a,b, the optical acceleration exerted onto nanoparticle #2 is shown for both polarizations. When the polarization is parallel to the axis connecting the pair, the nanoparticles tend to attract each other. This attraction increases significantly for decreasing nanoparticle distance. In the case of perpendicular polarization, the nanoparticles tend to attract each other at a large distance. However, as the nanoparticles get closer, they tend to repel each other strongly. For larger distances, the gradient force dominates. In contrast, the coupling force dominates when the two nanoparticles get closer, and the two nanoparticles repel each other. Therefore, we expect that the polarization of the incident light field plays a crucial role in the final arrangement of the nanoparticles.

In the next step, we seek to calculate the time it takes for a pair of nanoparticles, illuminated under parallel polarization, to collide. This step helps us identifying the timescales relevant to the experiment. Like in the previous paragraph, we assume the initial arrangement of the pair to be symmetric with respect to the center of the beam focus. For the dynamic calculations, we use the backward Euler method for the velocity in the time discretization of the Newtonian equation of motion and the drag force. This method is numerically stable for viscous environments. The velocity $\mathbf{v}$ and position $\mathbf{p}$ of the nanoparticles are calculated through the following equations:

$$\mathbf{v}(t + dt) = \mathbf{v}(t) + dt \times \mathbf{F}/m = \mathbf{v}(t) + dt \times [\mathbf{F}_d(t + dt) + \mathbf{F}_{opt}(t)]/m \tag{5}$$

$$\mathbf{p}(t + dt) = \mathbf{p}(t) + dt \times \mathbf{v}(t) \tag{6}$$

ADVANCED
SCIENCE NEWS
www.advancedsciencenews.com

LASER
& PHOTONICS
REVIEWS
www.lpr-journal.org

Figure 7. Dynamics of a platinum nanoparticle pair embedded in water in a Gaussian beam. The exerted acceleration on the second nanoparticle for polarization a) parallel to and b) perpendicular to the dimer axis as a function of the surface-to-surface distance of the nanoparticles. Nanoparticles with a radius of 10 nm (dashed) and 50 nm (solid) are considered. c) Exerted acceleration on the second nanoparticle as a function of the Gaussian beam power. d) The time for a collision of the dimer (for parallel polarization) as a function of water viscosity and the nanoparticles' surface to surface distance. We consider 2.5 mW optical power of a fundamental transverse Gaussian beam with a beam waist of 340 nm and a center wavelength of $\lambda = 780$ nm. The particles are embedded in water (with refractive index $n = 1.33$).

where $\mathbf{F}_{opt}$ is the optical force, $\mathbf{F}_d$ is the drag force, and dt is the time increment step in the numerical calculations. We use a time step of dt = 1 μs to obtain numerically converged results. We further use a linear drag force according to

$$\mathbf{F}_d(t) = -6\,\pi\mu\,\mathbf{v}(t) \tag{7}$$

where μ is the viscosity. This approximation is justified for the small particle radii under investigation here. It is well known that the water viscosity decreases with increasing water temperature. In the range of 0 to 100 °C, the viscosity changes from 1.8 to 0.2 mPa s.[67] Figure 7d shows that the collision time for the pair is in the order of milliseconds. The results show that optical forces play a crucial role in the dynamics of the platinum nanospheres, irrespective of the temperature. The larger the water temperature, the stronger the effect. For room temperatures (where $\mu \approx 1$ mPa s), nanoparticles at a distance of roughly 100–150 nm are subject to especially strong interactions. We note that this finding is in line with the pattern formation discussed in the previous section.

4. Discussion

The in situ experimental data presented above have shown several different time scales relevant to the process at stake and have revealed surprisingly fast and sudden events within the writing

laser focus. In the simulation section, we have quantified the light-induced forces at work under the conditions of our experiments. However, these are not necessarily the only forces at work. For example, previous work has pointed to the importance of heating effects.[47,68,69]

On this basis, in what follows, we aim at drawing a qualitative picture of the processes at work in the multi-photon laser printing of platinum that is consistent with all of the above data. This picture is schematically illustrated in **Figure 8**.

It is clear that the photo-reduction of the metal salt can start only after the writing laser has been switched on. Platinum ions are reduced to platinum atoms and are expected to form nanoclusters and/or nanoparticles. These particles are initially tiny and do not significantly contribute to the in situ reflectance signals shown in Figure 2. With increasing time of laser illumination, we expect that the particles within the laser focus grow in quantity and size (Figure 8a). They may also aggregate together to form larger particles. Optical forces can be remarkably effective in promoting the attraction of particles to each other from large distances (Figure 7). At some point, they have become so large that they lead to an appreciably large reflectance signal (Figure 2). At this point, it is decisive whether the particle adheres to the substrate or not. Let us discuss the two scenarios separately.

If the particle adheres to the substrate by covalent forces (Figure 8b), it may grow and act as a seed for further particles to aggregate on. This process leads to the rapid increase of the reflectance
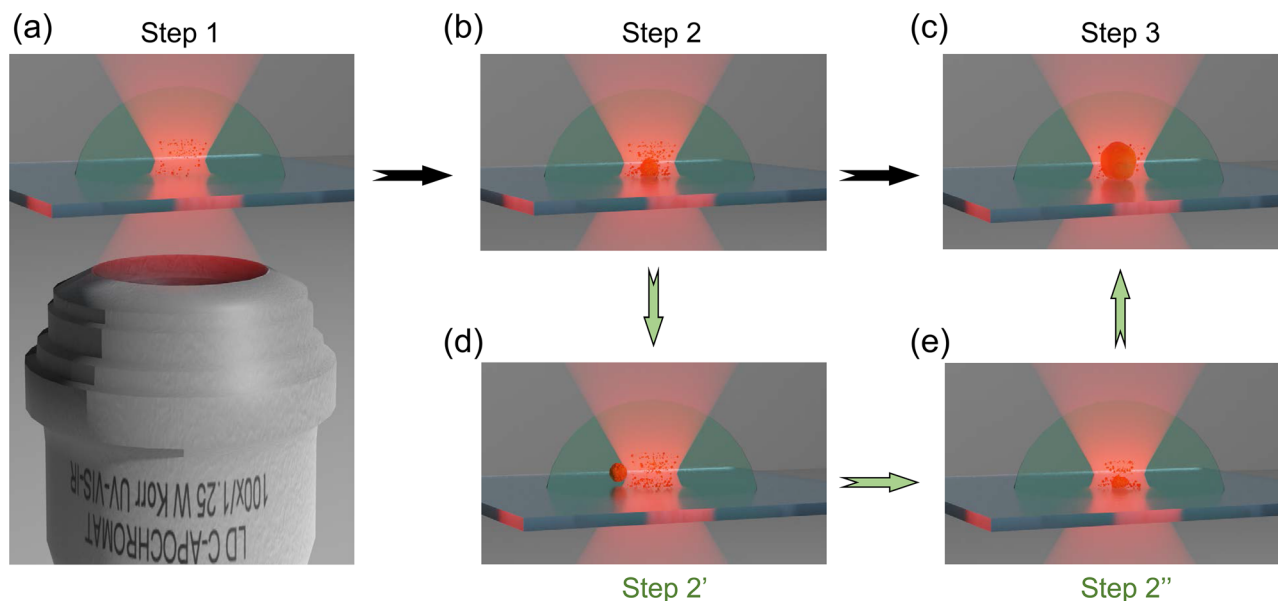
Figure 8. Scheme of the processes in laser printing of platinum. a) With increasing time of laser illumination, platinum particles grow in quantity and size in the focal volume. b) Platinum nanoparticles aggregate together to form a larger particle. At some point, reflectance from this larger particle is detected. c) If the particle formed in (b) sticks to the substrate by covalent forces, it may grow and act as a seed for further particles to aggregate on. As a result, a rapid increase of the reflectance signal is detected. After some hundreds of milliseconds, the particle reaches a size comparable to that of the writing laser focus and we observe a plateau of the reflectance signal. d) However, if the particle does not adhere sufficiently to the substrate, it may be ejected from the focal region, leading to a rapid drop of the in situ reflectance signal. Thus, a sharp spike is generated. Such ejection processes can happen several times. e) Eventually, a particle adheres stably onto the substrate and serves as a seed for the formation of a printed structure as shown in (c).

signal, e.g., in Figure 2a. Thereafter, the particle grows further. After some hundreds of milliseconds, the particle reaches a size comparable to that of the writing laser focus and we observe a plateau of the reflectance signal (Figure 8c). At this point, the particle has become opaque to light and casts a shadow, such that the photo-reduction rate drastically decreases, even if the writing laser is still switched on. The absorption of the writing laser in the platinum particle will heat the particle and enable further reduction by thermal processes, albeit at a small growth rate of the particle. The heating also fixes the nanoparticle to the substrate, a process that has been discussed in detail earlier.[70] Temperature-induced effects have also been discussed in References 47, 71, and 72. We also expect that this laser-induced heating sinters the individual nanoparticles mentioned above together. As a result, we obtain a platinum particle with spherical morphology (see inset of Figure 2a and Figure S5, Supporting Information) for properly chosen not-too-high writing laser power (around 35% P_0). For higher laser powers, the particle heating becomes so large that the surrounding water evaporates and forms micrometric bubbles that destroy the grown platinum structure and render the printed structures essentially useless.

Let us now discuss the case where the initial particle in Figure 8b does not adhere sufficiently to the substrate by covalent forces (Figure 8d). It may thus be ejected from the focal region, leading to a rapid drop of the in situ reflectance signal (see, e.g., Figure 2b). This process corresponds to the sharp peaks in Figure 2c–f. Notably, the signal fall times associated to the ejection processes, which happen on the scale of some tens of microseconds (Figure 3d), are orders of magnitude shorter than the other

timescales involved (Figure 3a–c). We see two possible origins for the rapid ejection processes. First, the discussed heating of particles may lead to turbulences that eject the particles from the focal region. Without turbulence, it is hard to conceive that thermal gradients alone lead to such rapid ejection processes of platinum particles. Second, light-induced forces, especially the scattering force or light pressure discussed in the simulation section may be responsible. After all, we have shown that particles with a radius around 100 nm experience a particularly large optical acceleration (see Figure 6a). Independent on the exact mechanism for the ejection of the particle, the particle is afterward no longer available in the focal region, and the process has to start from scratch. Such ejection processes can happen several times (Figure 2b) before a particle eventually covalently binds to the substrate surface (Figure 8e). This particle then serves as a seed for the further process. Clearly, the ejection processes depend on the viscosity of the surrounding medium. Consistent with our interpretation, Reference 39 recently obtained improved metal (silver) printing quality by using gelatin instead of water. To further test our interpretation in terms of a seed, we have performed additional point-exposure experiments. Here, we start from a preexisting platinum particle rather than from the bare glass substrate (Figure S6, Supporting Information). The writing laser and the probe laser are directly focused on this particle. Before the writing laser is switched on, a reflectance signal from the particle is already detected. After switching on the writing laser, the reflectance rapidly increases toward a plateau—with a negligible incubation period and without any spikes on the reflectance versus time.

ADVANCED
SCIENCE NEWS

www.advancedsciencenews.com

LASER
& PHOTONICS
REVIEWS

www.lpr-journal.org

In addition, to show the importance of the adhesion of the seed particle on the substrate, we have also performed writing experiments on a nonsilanized plasma-treated glass substrate as a control experiment (Figure S7, Supporting Information). Due to the weak adhesion of platinum particles, an initially formed particle cannot adhere to the substrate to resist the optical and turbulence forces. Therefore, even within a monitoring period as large as 9 s, the reflectance signal does not reach a steady plateau. Instead, only spikes are observed. Furthermore, from the online CCD camera image, no dominant platinum particle is observed at the focus position. Instead, randomly distributed particles occur in the periphery of the focus. Following our above interpretation, all of these particles have been ejected from the writing laser focus.

Let us now turn our attention to line exposures instead of point exposures. We start our discussion with low laser powers and then move to higher powers. At low powers, we observe pronounced polarization-dependent effects, as illustrated in Figure 5. As already pointed out in the results section, the mere observation of stripe structures, the orientation of which positively correlates with the orientation of the linear laser polarization (Figure 5) is evidence for light-induced forces. In the simulation section, we have shown calculated optical forces between two platinum spherical nanoparticles under the conditions of our writing experiments. We have found that nanoparticle pairs oriented along the axis of the electric-field vector of light experience an appreciably large attractive force and that nanoparticle pairs oriented perpendicular to the polarization axis of light experience a repulsive force. While these model calculations qualitatively explain the stripe structures in Figure 5, the overall behavior is much more complex. The light induces electric dipoles into many platinum nanoparticles, leading to a complex dipole-dipole interaction and resulting in complex nonlinear dynamics. The quantitative treatment of this problem is far beyond the scope of this paper.

At somewhat higher laser powers (see, e.g., Figure S4c,d Supporting Information) the polarization-dependent stripes are smeared out as already addressed in the section on experimental results. Furthermore, the line width increases somewhat (Figure S3, Supporting Information, 1 µm s^{-1} and 15% to 25% P_0). We attribute this behavior to photoreduction in the tails of the focus, which are not yet shadowed by the already printed line, and, possibly, to thermally induced reduction arising from laser heating due to absorption of light by the already printed line. For yet higher laser powers (Figure S3, Supporting Information, 1 µm s^{-1} and 30% to 50% P_0), we observe the formation of a large number of irregularly spaced bumps on top of the lines. We attribute these bumps to bubbles forming due to yet further heating of the metal line, leading to local evaporation of the water. The light-induced forces discussed above for low laser powers only play a minor role compared to thermal effects at such high laser powers.

5. Conclusions

We have presented systematic in situ diagnostics during platinum laser printing experiments by monitoring the backscattered light of a separate weak continuous-wave probe laser. We have identified three different time scales involved: 1) an incubation period in the range of some hundreds of milliseconds, 2) particle growth on the scale of few tens of milliseconds, and 3) particle ejection from the focal region on a scale of few tens of microseconds. We have shown that the scattering force or light pressure is a possible source for driving these ejections. Optical forces are also responsible for stripes on the printed platinum surfaces that are oriented along the polarization of the writing laser. These findings can qualitatively be explained by simulations of the optical forces between adjacent platinum nanoparticles in the viscous water environment. With this improved understanding of the underlying processes and timescales, we expect to see enhanced capability and printing quality in future developments of metal laser nanoprinting.

6. Experimental Section

Pt Ink: Ammonium trisoxalatoferrate (III) trihydrate and ammonium tetrachloroplatinate (II) were purchased from Sigma Aldrich. $(NH_4)_3[Fe(C_2O_4)_3]\cdot3H_2O$ (0.5 M) and $(NH_4)_2[PtCl_4]$ (0.07 M) aqueous solution were prepared and stored in the dark at 4 °C. The Platinum based ink (1:1 by volume $(NH_4)_3[Fe(C_2O_4)_3]:(NH_4)_2[PtCl_4]$) was always freshly prepared prior to the laser experiments.

Sample Preparation: For the preparation of samples, precision cover glasses were first carefully cleaned with water, acetone, isopropanol successively. Then, the cover glasses were kept in an oven at 150 °C for 1 h to get rid of water on the surface and treated with oxygen plasma for 10 min. The cleaned cover glasses were placed in vials containing a solution of (3-aminopropyl) triethoxysilane dissolved in toluene (0.2% vol) for 60 min at ambient temperature. Finally, the cover glass was washed successively with toluene, acetone, isopropanol, and finally dried in a stream of nitrogen. The silanization process was performed to better bind the platinum particles to the amino-functionalized substrate surface during the laser reduction process. Silanized glass cover slips were placed in the sample holder, and a polydimethylsiloxane (PDMS) ring with a height of close to 1 mm was used as a reservoir. A droplet of ink was placed in the middle of the PDMS ring and the top was covered with a second PDMS piece to prevent any evaporation of solvent during the fabrication process. In point exposure experiments, to quantitatively estimate the reflectance signal, the silanized cover glass was partially coated with a 120 nm gold layer with evaporation coating (Cressington 108). The central part of the cover glass was covered with polyimide tape (PIT0.5S-UT, LINQTAPE) to keep it uncoated. The reflectance from the platinum particle was calibrated with the full reflection, which was calculated by the reflection from the glass–gold interface.

Instrumentation and Metal Reduction: A Ti:Sa femtosecond laser (Coherent Chameleon Ultra II) was used for multi-photon excitation. A diode laser (675 nm wavelength, Thorlabs) was adopted as a probe laser. These two laser sources were combined with a dichroic mirror and focused into Pt ink by a water objective lens (Zeiss LD C-APOCHROMAT 100 × /1.25 W, numerical aperture NA = 1.25). The objective was mounted by a piezoelectric stage (Physik Instrumente P-733.ZCL) with 100 µm travel to translate the focus along the optical axis. The sample was translated horizontally using a 2D piezo stage (Physik Instrumente P-734.2CL) with 100 µm × 100 µm travel. The 2D stage was mounted on top of another stage (Physik Instrumente P-M-686) with 25 mm × 25 mm travel for coarse movement. The backscattered signal from a photo-induced Pt particles was collected with a photodiode (FDS1010, Thorlabs). The rise time of the photodiode was 65 ns. A 675 nm band-pass filter (Chroma Technology) was placed in front of the photodiode to avoid possible crosstalk from the fs laser. The switching and power of the fs laser were controlled by acousto-optic modulators (AOMs, AA Opto Electronic MTS40-A3–750.850). The AOM response time was about 500 ns. All laser powers were measured at the position of the objective lens' entrance pupil. A power of 3.5 mW corresponding to 100% was used in all the experiments. A half-wave plate

adjusted the linear laser polarization direction. An oscilloscope (Rohde & Schwarz, RTO 1024) was used to collect the signal sent to AOM and the signal collected by a photodiode. During the writing procedure, the probe laser was also used to find the z-direction of the glass-ink interface with high accuracy via a confocal detection scheme. In the interface-finding process, the focus was scanned with respect to the glass substrate along the z-direction in a range of a few micrometers. A maximum of the reflected signal occurred when focus and interface were aligned. The position of this maximum and hence the position of the glass substrate interface by an accuracy below 10 nm were determined. A camera and a light illumination in transmission by a red light-emitting diode were used to monitor the exposure process in situ. After the writing was completed, the samples were washed for 5 min in pure water and blow dried gently with nitrogen gas.

Characterization: The surface morphologies of the samples were measured on a Zeiss Leo 1530 scanning electron microscope operating at 10.0 keV. The samples were coated with an 8 nm gold layer prior to measurements.

Supporting Information

Supporting Information is available from the Wiley Online Library or from the author.

Acknowledgements

Conflict of Interest

The authors declare no conflict of interest.

Data Availability Statement

The data underlying the plots within this paper, Supporting Information and related 3D printing files are published on the open-access data repository of the Karlsruhe Institute of Technology (https://doi.org/10.5445/IR/1000140839).

Keywords

[1] M. Carlotti, V. Mattoli, *Small* **2019**, *15*, 1902687.

[2] J. Fischer, M. Wegener, *Laser Photonics Rev.* **2013**, *7*, 22.

[3] Z. S. Gan, M. D. Turner, M. Gu, *Sci. Adv.* **2016**, *2*, e1600084.

[4] T. Gissibl, S. Thiele, A. Herkommer, H. Giessen, *Nat. Commun.* **2016**, *7*, 11763.

[5] J. Li, J. Mu, B. Wang, W. Ding, J. Liu, H. Guo, W. Li, C. Gu, Z. Li, *Laser Photonics Rev.* **2014**, *8*, 602.

[6] T. Frenzel, M. Kadic, M. Wegener, *Science* **2017**, *358*, 1072.

[7] D. W. Yee, M. L. Lifson, B. W. Edwards, J. R. Greer, *Adv. Mater.* **2019**, *31*, 1901345.

[8] I. Bellis, S. Nocentini, M. G. D. Santi, D. Martella, C. Parmeggiani, S. Zanotto, D. S. Wiersma, *Laser Photonics Rev.* **2021**, *15*, 202100090.

[9] D. Serien, S. Takeuchi, *ACS Biomater. Sci. Eng.* **2017**, *3*, 487.

[10] M. Hippler, K. Weissenbruch, K. Richler, E. D. Lemma, M. Nakahata, B. Richter, C. Barner-Kowollik, Y. Takashima, A. Harada, E. Blasco, M. Wegener, M. Tanaka, M. Bastmeyer, *Sci. Adv.* **2020**, *6*, eabc2648.

[11] H. Zeng, P. Wasylczyk, C. Parmeggiani, D. Martella, M. Burresi, D. S. Wiersma, *Adv. Mater.* **2015**, *27*, 3883.

[12] H. Ceylan, I. C. Yasa, O. Yasa, A. F. Tabak, J. Giltinan, M. Sitti, *ACS Nano* **2019**, *13*, 3353.

[13] S. Jeon, S. Kim, S. Ha, S. Lee, E. Kim, S. Y. Kim, S. H. Park, J. H. Jeon, S. W. Kim, C. Moon, B. J. Nelson, J. Y. Kim, S. W. Yu, H. Choi, *Sci. Rob.* **2019**, *4*, eaav4317.

[14] C. Xin, L. Yang, J. W. Li, Y. L. Hu, D. D. Qian, S. Y. Fan, K. Hu, Z. Cai, H. Wu, D. W. Wang, D. Wu, J. R. Chu, *Adv. Mater.* **2019**, *31*, 1808226.

[15] L. Yang, X. Chen, L. Wang, Z. Hu, C. Xin, M. Hippler, W. Zhu, Y. Hu, J. Li, Y. Wang, L. Zhang, D. Wu, J. Chu, *Adv. Funct. Mater.* **2019**, *29*, 1905745.

[16] A. C. Lamont, M. A. Restaino, M. J. Kim, R. D. Sochol, *Lab Chip* **2019**, *19*, 2340.

[17] F. Mayer, S. Richter, J. Westhauser, E. Blasco, C. Barner-Kowollik, M. Wegener, *Sci. Adv.* **2019**, *5*, eaau9160.

[18] Z. C. Ma, Y. L. Zhang, B. Han, X. Y. Hu, C. H. Li, Q. D. Chen, H. B. Sun, *Nat. Commun.* **2020**, *11*, 4536.

[19] Z. C. Ma, Y. L. Zhang, B. Han, Q. D. Chen, H. B. Sun, *Small Methods* **2018**, *2*, 1700413.

[20] E. H. Waller, S. Dix, J. Gutsche, A. Widera, G. von Freymann, *Micromachines* **2019**, *10*, 827.

[21] T. Tanaka, A. Ishikawa, S. Kawata, *Appl. Phys. Lett.* **2006**, *88*, 081107.

[22] M. M. Hossain, M. Gu, *Laser Photonics Rev.* **2014**, *8*, 233.

[23] S. Shukla, X. Vidal, E. P. Furlani, M. T. Swihart, K. T. Kim, Y. K. Yoon, A. Urbas, P. N. Prasad, *ACS Nano* **2011**, *5*, 1947.

[24] W.-E. Lu, Y.-L. Zhang, M.-L. Zheng, Y.-P. Jia, J. Liu, X.-Z. Dong, Z.-S. Zhao, C.-B. Li, Y. Xia, T.-C. Ye, X.-M. Duan, *Opt. Mater. Express* **2013**, *3*, 1660.

[25] E. Blasco, J. Muller, P. Muller, V. Trouillet, M. Schon, T. Scherer, C. Barner-Kowollik, M. Wegener, *Adv. Mater.* **2016**, *28*, 3592.

[26] M. R. Lee, H. K. Lee, Y. J. Yang, C. S. L. Koh, C. L. Lay, Y. H. Lee, I. Y. Phang, X. Y. Ling, *ACS Appl. Mater. Interfaces* **2017**, *9*, 39584.

[27] M. Machida, T. Niidome, H. Onoe, A. Heisterkamp, M. Terakawa, *Opt. Express* **2019**, *27*, 14657.

[28] A. Ishikawa, T. Tanakaa, S. Kawata, *Appl. Phys. Lett.* **2006**, *89*, 113102.

[29] Y. Y. Cao, N. Takeyasu, T. Tanaka, X. M. Duan, S. Kawata, *Small* **2009**, *5*, 1144.

[30] B. B. Xu, H. Xia, L. G. Niu, Y. L. Zhang, K. Sun, Q. D. Chen, Y. Xu, Z. Q. Lv, Z. H. Li, H. Misawa, H. B. Sun, *Small* **2010**, *6*, 1762.

[31] R. Ameloot, M. B. J. Roeffaers, G. De Cremer, F. Vermoortele, J. Hofkens, B. F. Sels, D. E. De Vos, *Adv. Mater.* **2011**, *23*, 1788.

[32] B. B. Xu, L. Wang, Z. C. Ma, R. Zhang, Q. D. Chen, C. Lv, B. Han, X. Z. Xiao, X. L. Zhang, Y. L. Zhang, K. Ueno, H. Misawa, H. B. Sun, *ACS Nano* **2014**, *8*, 668.

[33] S. Kang, S. Vora, E. Mazur, *Nanotechnology* **2015**, *26*, 121001.

[34] Y. L. Sun, Q. Li, S. M. Sun, J. C. Huang, B. Y. Zheng, Q. D. Chen, Z. Z. Shao, H. B. Sun, *Nat. Commun.* **2015**, *6*, 8612.

[35] M. Terakawa, M. L. Torres-Mapa, A. Takami, D. Heinemann, N. N. Nedyalkov, Y. Nakajima, A. Hordt, T. Ripken, A. Heisterkamp, *Opt. Lett.* **2016**, *41*, 1392.

[36] P. Barton, S. Mukherjee, J. Prabha, B. W. Boudouris, L. Pan, X. F. Xu, *Nanotechnology* **2017**, *28*, 505302.

[37] K. Vora, S.-Y. Kang, S. Shukla, E. Mazur, *Appl. Phys. Lett.* **2012**, *100*, 063120.

[38] M. Machida, Y. Nakajima, M. L. Torres-Mapa, D. Heinemann, A. Heisterkamp, M. Terakawa, **2018**, *8*, 187.

[39] E. H. Waller, J. Karst, G. Freymann, *Light Adv. Manuf.* **2021**, *2*, 8.

[40] L. D. Zarzar, B. S. Swartzentruber, J. C. Harper, D. R. Dunphy, C. J. Brinker, J. Aizenberg, B. Kaehr, *J. Am. Chem. Soc.* **2012**, *134*, 4007.

[41] E. Greenberg, N. Armon, O. Kapon, M. Ben-Ishai, H. Shpaisman, *Adv. Mater. Interfaces* **2019**, *6*, 1900541.

[42] Z.-C. Ma, Y.-L. Zhang, B. Han, X.-Q. Liu, H.-Z. Zhang, Q.-D. Chen, H.-B. Sun, *Adv. Mater. Technol.* **2017**, *2*, 1600270.

[43] X. Yang, M. Sun, Y. Bian, X. He, *Adv. Funct. Mater.* **2019**, *29*, 1807615.

[44] E. J. Bjerneld, K. V. G. K. Murty, J. Prikulis, M. Kall, *Chem. Phys. Chem.* **2002**, *3*, 116.

[45] M. Bellec, A. Royon, B. Bousquet, K. Bourhis, M. Treguer, T. Cardinal, M. Richardson, L. Canioni, *Opt. Express* **2009**, *17*, 10304.

[46] S. J. Lee, B. D. Piorek, C. D. Meinhart, M. Moskovits, *Nano Lett.* **2010**, *10*, 1329.

[47] S. Hashimoto, D. Werner, T. Uwada, *J. Photochem. Photobiol. C* **2012**, *13*, 28.

[48] T. Ritacco, P. Pagliusi, M. Giocondo, *Colloids Surf. A Physicochem. Eng. Asp.* **2021**, *610*, 125927.

[49] J. B. Mueller, J. Fischer, F. Mayer, M. Kadic, M. Wegener, *Adv. Mater.* **2014**, *26*, 6566.

[50] J. Fischer, J. B. Mueller, A. S. Quick, J. Kaschke, C. Barner-Kowollik, M. Wegener, *Adv. Opt. Mater.* **2015**, *3*, 221.

[51] Y. Nakazato, K. Taniguchi, S. Ono, T. Eitokua, K. Katayama, *Phys. Chem. Chem. Phys.* **2009**, *11*, 10064.

[52] S. Ibrahimkutty, P. Wagener, T. dos Santos Rolo, D. Karpov, A. Menzel, T. Baumbach, S. Barcikowski, A. Plech, *Sci. Rep.* **2015**, *5*, 16313.

[53] K. M. McPeak, S. V. Jayanti, S. J. P. Kress, S. Meyer, S. Iotti, A. Rossinelli, D. J. Norris, *ACS Photonics* **2015**, *2*, 326.

[54] L. Yang, F. Mayer, U. H. F. Bunz, E. Blasco, M. Wegener, *Light Adv. Manuf.* **2021**, *2*, 17.

[55] J. P. Barton, D. R. Alexander, S. A. Schaub, *J. Appl. Phys.* **1989**, *66*, 4594.

[56] Y. L. Xu, *Appl. Opt.* **1995**, *34*, 4573.

[57] A. Rahimzadegan, R. Alaee, I. Fernandez-Corbaton, C. Rockstuhl, *Phys. Rev. B* **2017**, *95*, 035106.

[58] G. Mie, *Ann. Phys.* **1908**, *330*, 377.

[59] C. F. Bohren, D. R. Huffman, *Absorption and Scattering of Light by Small Particles*, John Wiley & Sons, New York **2008**.

[60] Y. I. Salamin, *Appl. Phys. B* **2006**, *86*, 319.

[61] J. P. Barton, D. R. Alexander, *J. Appl. Phys.* **1989**, *66*, 2800.

[62] J. A. Lock, *Appl. Opt.* **2004**, *43*, 2545.

[63] W. S. M. Werner, K. Glantschnig, C. Ambrosch-Draxl, *J. Phys. Chem. Ref. Data* **2009**, *38*, 1013.

[64] Platinum, national library of medicine, national center for biotechnology information, https://pubchem.ncbi.nlm.nih.gov/compound/Platinum (accessed: June 2021).

[65] R. Alaee, C. Rockstuhl, I. Fernandez-Corbaton, *Adv. Opt. Mater.* **2019**, *7*, 1800783.

[66] A. Rahimzadegan, T. D. Karamanos, R. Alaee, A. G. Lamprianidis, D. Beutel, R. W. Boyd, C. Rockstuhl (Preprint). arXiv:2108.12364, v2, unpublished.

[67] The international association for the properties of water and steam, http://www.iapws.org/relguide/viscosity.html (accessed: June 2021).

[68] C. J. Rodrigues, J. A. Bobb, M. G. John, S. P. Fisenko, M. S. El-Shall, K. M. Tibbetts, *Phys. Chem. Chem. Phys.* **2018**, *20*, 28465.

[69] C. Kindle, A. Castonguay, S. McGee, J. A. Tomko, P. E. Hopkins, L. D. Zarzar, *ACS Appl. Nano Mater.* **2019**, *2*, 2581.

[70] S. Ito, H. Yoshikawa, H. Masuhara, *Appl. Phys. Lett.* **2002**, *80*, 482.

[71] S. Ito, T. Mizuno, H. Yoshikawa, H. Masuhara, *Jpn. J. Appl. Phys.* **2007**, *46*, L241.

[72] K. Setoura, S. Ito, H. Miyasaka, *Nanoscale* **2017**, *9*, 719.